Catalysis Today 314 (2018) 28–41

Contents lists available at ScienceDirect

Catalysis Today

journal homepage: www.elsevier.com/locate/cattod

Preparation of perovskites $PbBiO_2I$/PbO exhibiting visible-light photocatalytic activity

Fu-Yu Liu, Jia-Hao Lin, Yong-Ming Dai, Li-Wen Chen, Shiuh-Tsuen Huang, Tsung-Wen Yeh, Jia-Lin Chang, Chiing-Chang Chen*

Department of Science Education and Application, National Taichung University of Education, Taichung 403, Taiwan

ARTICLE INFO

Keywords:
$PbBiO_2I$
PbO
Photocatalytic
Crystal violet
2-Hydroxybenzoic acid

ABSTRACT

The first synthetic study on $PbBiO_2I$/PbO nanocomposite preparation using a controlled hydrothermal method is reported. The morphologies and composition of the samples are controlled by adjusting some parameters, including reaction pH, Pb/Bi molar ratio, and temperature. All the samples are characterized by XRD, TEM, XPS, SEM-EDS, PL, BET, EPR, and UV–vis-DRS. The photodegradation activities are evaluated against the de-colorization of crystal violet (CV) and 2-hydroxybenzoic acid (2-HBA) in aqueous solution under visible light illumination. In particular, the catalytic performance illustrates the best reaction rate constant $1.159 \times 10^{-1}\,h^{-1}$ once $PbBiO_2I$/PbO is used as the photocatalyst for the degradation of CV; which is 3 and 20 times higher than the reaction rate constants of $PbBiO_2I$ and PbO being the photocatalysts, respectively. This study reveals that $PbBiO_2I$/PbO can be used for repressing the recombination of photo-generated electron-hole pairs and contribute to the enhanced photocatalytic activity of semiconductors in the visible-light-driven catalysis. The possible photocatalytic degradation mechanism is studied by using different active species through EPR and adding suitable scavengers. When being irradiated, two major active species, O_2^- and $^1O_2$, and a minor active species, h^+, can be produced for the CV degradation.

1. Introduction

The elimination of toxic chemicals from wastewater has become one of the most crucial aspects of contemporary pollution-control methods because of the hazardous effects of these chemicals on living beings and the environment. In face of an increasingly serious environmental pollution and energy crunch, photocatalysis, as a suitable technology, plays an important role in the degradation of pollutants and solar energy conversion [1,2]. For the practical applications of photocatalysis, an environmentally powerful and cheap photocatalyst is regarded as an important component [3]. CV, a cationic triphenylmethane dye, is found the use as colorants in industry and as antimicrobial agents [4]. However, great trouble about the thyroid peroxidase-catalyzed oxidation of the triphenylmethane class of dyes is arisen because the reactions might produce various *N*-de-alkylated primary and secondary aromatic amines, with the structures similar to aromatic amine carcinogens [5]. Photocatalytic degradation of CV has been studied using several systems to generate active species, including heterojunctions BiOI/g-C_3N_4 [6], BiOI/GO [7], $SrFeO_{3-x}$/g-C_3N_4 [8], BiOCl/BiOBr [9], BiOBr/$PbBiO_2Br$ [10], etc. and pure semiconductors $Bi_xAg_yO_z$ [11], Bi_2WO_6 [12], TiO_2 [13], etc.

Recently, Bi-based oxyhalides have drawn people's attention to their potential application as novel photocatalysts owing to their unique layered structures and high chemical stabilities [13,14,15]. Bi-based layered structure compounds, within Aurivillius family such as BiOX (X = Cl, Br, I) [9,16–18], Bi_2WO_6 [19], $Bi_4Ti_3O_{12}$ [20], $BiVO_4$ [21], etc., have been extensively explored as highly efficient photo-catalysts due to their unique layered structure and high catalytic activity. It is thought that the Bi 6 s and O 2p levels can make a largely dispersed hybridized valence band, which favors the mobility of photo-generated holes and the oxidation reaction of inducing efficient separation of photo-generated electron-hole pairs and then improving the photocatalytic efficiency [22].

Many inorganic materials have modular structures, where the individual units are responsible for different functions. Sillen's phases are an adaptive structure series of oxyhalides originally investigated by Sillen et al. in the 1940's [24]. The structures of these compounds consist of $[M_2O_2]$ layers (M = Pb, Bi, Cd, Ba, Sr) intermixed with either halogen or metal halogen layers. Two examples of these phases are $PbBiO_2I$ which consist of $[M_2O_2]$ with 2 halogens and $[M_2O_2]$ with 1 halogen layer, respectively. The Aurivillius intergrowth phases consist of perovskite blocks sandwiched between the $[Bi_2O_2]^{2+}$ slabs and can

* Corresponding author.
E-mail address: ccchen@mail.ntcu.edu.tw (C.-C. Chen).

https://doi.org/10.1016/j.cattod.2018.02.006
Received 29 September 2017; Received in revised form 30 January 2018; Accepted 2 February 2018
Available online 12 February 2018

be described with a general formula $[Bi_2O_2]$- $A_{n-1}B_nO_{3n+1}$, where A is a large alkali, alkali-earth, rare-earth, or Pb^{2+} cation, and B is a d^0 transition metal cation, such as Nb^{5+}, W^{6+}, Ta^{5+}, or Ti^{4+} [23]. The extended Bi-based oxychlorides are the Sillen–Aurivillius intergrowth $[Bi_2O_2][A_{n-1}B_nO_{3n+1}][Bi_2O_2][Cl_m]$ [13,15], where the Aurivillius family $[Bi_2O_2][A_{n-1}B_nO_{3n+1}]$ is inter-grown with the structure-similarity of Sillen family $[Bi_2O_2][Cl_m]$, $X_m]$, where n is the number of perovskite layers and m is the number of halide layers, such as Bi_4TaO_8Cl, Bi_4NbO_8Cl, etc. These oxychloride compounds are of interest as selective oxidation catalysts [13], ferroelectric materials [15] and pigments [25].

The $[Bi_2O_2]^{2+}$ slabs with the α-PbO type structure as well as simple halide layers are effective spacers in some layered functional materials [23,26]. Previous reports mainly discussed the electronic reasons for the different photocatalytic activity of layered $PbBiO_2X$-type materials (X = Cl, Br, I) [10,27–30]. However, crystal-chemical arguments should also be taken into consideration to explain the photocatalytic properties of the compounds. A possible reason for the different catalytic activity of the oxides may be derived collectively from their crystal structures, their optic, and their redox properties. All the solid materials under discussion crystallize in a layered structure. They exhibit covalent metal oxygen layers $[PbBiO_2]^+$ separated by halide layers, which are stacked along [001]. One can assume that the crystal surface consists of metal oxygen layers, i.e., the metal atoms are expected to form the (001) surfaces [26]. In the case of bismuth compounds, the metal position was statistically occupied by lead and bismuth with the ratio 1:1 [31,32]. It was reported that the band gaps of $PbBiO_2I$ [27,33], $PbBiO_2Br$ [10,28,34,35], and $PbBiO_2Cl$ [29,36,37] were 2.39, 2.47, and 2.53 eV, respectively. It seemed that the gaps of all these semiconductors were in the visible-light range to catalyze the photocatalytic reaction.

So as to narrow the band gap (*Eg*) of BiOX and enhance the visible light-driven activity of the catalyst, we incorporated Pb^{2+} into $[Bi_2O_2]$ layers based on the structure of BiOX to form the derived compound of $PbBiO_2X$ [10,38]. $PbBiO_2X$ is supposed to show a narrower *Eg* than BiOX. Because the contribution of Pb $6s^2$ orbitals occupy higher energy states at the valence band maximum (VBM), and the contribution of Pb 6p orbitals occupy lower energy states at the conduction band minimum (CBM). The hybridized states of VBM and CBM can decrease the effective masses of holes and electrons, respectively, to favor a longer traveling distance for excited carriers. Just as expected, the experimentally evaluated E_g of $PbBiO_2X$ (X = Cl, Br, I; E_g = 2.53, 2.40, 2.29 eV) is much narrower than that of nano-metered BiOX (E_g = 3.38, 2.80, 2.57 eV) [6,10,30,38]. Then, the visible-light-response photocatalytic activity of the material is also higher than that of BiOX. In our judgment, the higher activity for photocatalytic degradation of dyes on $PbBiO_2X$ is not only attributed to the layered structure but also the hybridized band structure.

The development of visible-light-driven photocatalysts, as an alternative in toxic wastewater treatment, has recently obtained considerable attention. An effective and simple topic to improve the photocatalytic activity of a photocatalyst is the incorporation of a composite, because a composite has great potential for tuning the wished electronic properties of photocatalysts and efficiently separating the photogenerated electron–hole pairs. So far, a composite concerned $PbBiO_2Br$, such as $PbBiO_2Br/NbSe_2$ [39], $PbBiO_2Cl/BiOCl$ [38], and $PbBiO_2Br/BiOBr$ [10], has been reported and exhibited the enhanced photocatalytic activity.

Herein, we report another novel layered photocatalyst $PbBiO_2I$/PbO. To the best of our knowledge, nanocomposite semiconductors consisting of $PbBiO_2I$ and PbO have not yet been reported in the literature. This is the first report that $PbBiO_2I$/PbO composites are synthesized by a template-free hydrothermal method through degrading CV and 2-HBA in aqueous solution under visible-light irradiation. The photocatalytic efficiency of $PbBiO_2I$/PbO composites are further discussed.

2. Experimental details

2.1. Materials

CV dye (TCI), 2-hydroxybenzoic acid (salicylic acid), $Pb(NO_3)_2$·H_2O, ammonium oxalate (Osaka), $Bi(NO_3)_3$·$5H_2O$ (Katayama), *p*-benzoquinone (Alfa aesar), sodium azide (Sigma-Aldrich), and isopropanol (Merck) were purchased and used without further purification. Reagent-grade HNO_3, NaOH, CH_3COONH_4, and HPLC-grade methanol were obtained from Merck.

2.2. Instruments and analytical methods

The X-ray diffraction (XRD) patterns were recorded on a MAC Science MXP18 equipped with Cu-Kα radiation, operating at 40 kV and 80 mA. The field-emission transmission electron microscopy (FE-TEM) images, selected area electron diffraction (SAED) patterns, high resolution transmission electron microscopy (HRTEM) images, and energy-dispersive X-ray spectra (EDS) were obtained using JEOL-2010 with an accelerating voltage of 200 kV. The Brunauer-Emmett-Teller (BET) specific surface areas of the samples (S_{BET}) were measured with an automated system (Micrometrics Gemini) using nitrogen gas as the adsorbate at liquid nitrogen temperature. Field emission scanning electron microscopy-electron dispersive X-ray spectroscopy (FE-SEM-EDS) measurements were carried out using a JEOL JSM-7401F at an acceleration voltage of 15 kV. The Ultra-violet photoelectron spectroscopy (UPS) measurements were performed using ULVAC-PHI XPS, PHI Quantera SXM. UPS was used to measure the work function using He I emission (21.2 eV, ~50 W) as the source of ultra-violet-light, and the take-off angle was 90°. Specimens were biased at −7.5 V DC to give low-energy secondary electrons extra energy to overcome the work function of the detector (4.4 eV) for acquiring the onset of secondary electrons. The work function of specimens was extracted from the UPS data using the width of the spectra. High resolution X-ray photoelectron spectroscopy (HRXPS) measurements were carried out using ULVAC-PHI. Waters ZQ LC/MS system, equipped with a binary pump, a photodiode array detector, an autosampler, and a micromass detector, was used for separation and identification. The amount of residual dye at each reaction cycle was determined by HPLC–MS. The HPLC-PDA-ESI–MS system was composed a Waters 1525 binary pump, a 2998 photodiode-array-detector, and a 717 plus auto-sampler. Besides, a ZQ-2000 micro-mass detector and an Atlantis ™ dC18 column (250 mm × 4.6 mm i.d., dp = 5 μm) were used for separation and identification. The column effluent was introduced into the ESI source of the mass spectrometer.

The amount of residual dye at each reaction cycle was determined by HPLC-PDA-ESI–MS. The analysis of organic intermediates was accomplished by HPLC-PDA-ESI–MS after the readjustment of chromatographic conditions in order to make the mobile phase (Solvent A and B) compatible with the working conditions of the mass spectrometer. Solvent A was 25 mM aqueous ammonium acetate buffer (pH 6.9), and solvent B was methanol. LC was carried out on an Atlantis ™ dC18 column (250 mm × 4.6 mm i.d., dp = 5 μm). The mobile phase flow rate was 1.0 mL/min. A linear gradient was run as follows: t = 0, A = 95, B = 5; t = 20, A = 50, B = 50; t = 35–40, A = 10, B = 90; t = 45, A = 95, B = 5. The column effluent was introduced into the ESI source of the mass spectrometer. The quadruple mass spectrometer equipped with an ESI interface with heated nebulizer probe at 350 °C was used with an ion source temperature of 80 °C. ESI was carried out with the vaporizer at 350 °C and nitrogen as sheath (80 psi) and auxiliary (20 psi) gas to assist with the preliminary nebulization and to initiate the ionization process. A discharge current of 5 μA was applied. Tube lens and capillary voltage were optimized for the maximum response during the perfusion of the CV standard.

Table 1
Codes of as-prepared samples under different hydrothermal conditions. ($Pb(NO_3)_2$/$Bi(NO_3)_3$ = 1/3–3/3, KI = 1 mmol, pH = 1–13, temp = 150–250 °C, time = 12 h).

Temperature (°C)/Molar ratio (Pb:Bi)	pH value				
	1	4	7	10	13
150(1:3)	P1BI-150-1	P1BI-150-4	P1BI-150-7	P1BI-150-10	P1BI-150-13
150(3:3)	P3BI-150-1	P3BI-150-4	P3BI-150-7	P3BI-150-10	P3BI-150-13
200(1:3)	P1BI-200-1	P1BI-200-4	P1BI-200-7	P1BI-200-10	P1BI-200-13
200(3:3)	P3BI-200-1	P3BI-200-4	P3BI-200-7	P3BI-200-10	P3BI-200-13
250(1:3)	P1BI-250-1	P1BI-250-4	P1BI-250-7	P1BI-250-10	P1BI-250-13
250(3:3)	P3BI-250-1	P3BI-250-1	P3BI-250-7	P3BI-250-10	P3BI-250-13

2.3. Synthesis of $PbBiO_2I$/PbO

1, 3 mmol $Pb(NO_3)_2 \cdot H_2O$ and 3 mmol $Bi(NO_3)_3 \cdot 5H_2O$ were first mixed in a 50 mL flask and then added 30 mL H_2O. With continuous stirring, 2 M NaOH was added dropwise to adjust the pH = 1–14. The solution was then stirred vigorously for 30 min and 10 mL solution was transferred into a 30 mL Teflon-lined autoclave, which was heated up to 100–250 °C for 12 h and then naturally cooled down to room temperature. These resulted solid precipitate was collected by filtration, washed with deionized water and methanol to remove any possible ionic species in the solid precipitate, and then dried at 60 °C overnight. Depending on the $Pb(NO_3)_2 \cdot H_2O$/$Bi(NO_3)_3 \cdot 5H_2O$ molar ratio (1:3, 3:3), pH value, and reaction temperature, the samples were synthesized and labeled as shown in Table 1; the as-prepared samples were labeled from P1BI-150-1 to P3BI-250-13

2.4. Photocatalytic experiments

The CV (or 2-HBA) irradiation experiments were carried out on stirred aqueous solution contained in a 100-mL flask; the aqueous suspension of CV (or 2-HBA) (100 mL, 10 ppm) and the amount of catalyst powder were placed in a Pyrex flask. The pH of the suspension was adjusted by adding either NaOH or HNO_3 solution. Dark experiments were performed in order to examine the adsorption/desorption equilibrium. Mixing 10 mg of the photocatalyst with 100 mL CV (or 2-HBA) aqueous solution with a known initial concentration in a 100 mL flask, the mixture was shaken in an orbital shaker (100 rpm) at a constant temperature. The mixture was centrifuged at 3000 rpm in a centrifugation machine after batch sorption experiments so that the absorbance of CV (or 2-HBA) could be determined at 580 (or 300) nm by means of HPLC–MS. The concentrations of the solutions were determined using linear regression equation. Prior to the irradiation, the suspension was magnetically stirred in dark for ca. 30 min to establish an adsorption/desorption equilibrium between the CV (or 2-HBA) and the catalyst surface. The optical system for the catalytic reaction under visible-light includes a 150W Xe arc lamp, a reaction container and a cut-off filter (> 420 nm), with the light intensity fixed at 31.2 W/m^2 were used for irradiating the reaction vessel 30 cm away from the light source. At given irradiation time intervals, a 5-mL aliquot was collected and centrifuged to remove the catalyst. The supernatant was measured by HPLC–MS.

A different quencher was introduced to scavenge the relevant active species in order to evaluate the effect of the active species during the photocatalytic reaction. Active species, ·OH, $O_2 \cdot^-$, h^+, and $^1O_2$, were studied by adding 1.0 mM benzoquinone (BQ, a quencher of $O_2 \cdot^-$) [38], 1.0 mM sodium azide (SA, a quencher of $^1O_2$ [40], 1.0 mM isopropanol (IPA, a quencher of ·OH) [41], and 1.0 mM ammonium oxalate (AO, a quencher of h^+) [42], respectively. The method was similar to the former photocatalytic experiments [7,8].

3. Results and discussion

3.1. Characterization of as-prepared samples

3.1.1. XRD

Figs. 1 and S1 of supplementary data show the XRD patterns of the as-prepared samples; the patterns clearly show the existence of the composites *t*-$PbBiO_2I$/PbO, *t*-$PbBiO_2I$/Bi_2O_3, *t*-$PbBiO_2I$/PbO/

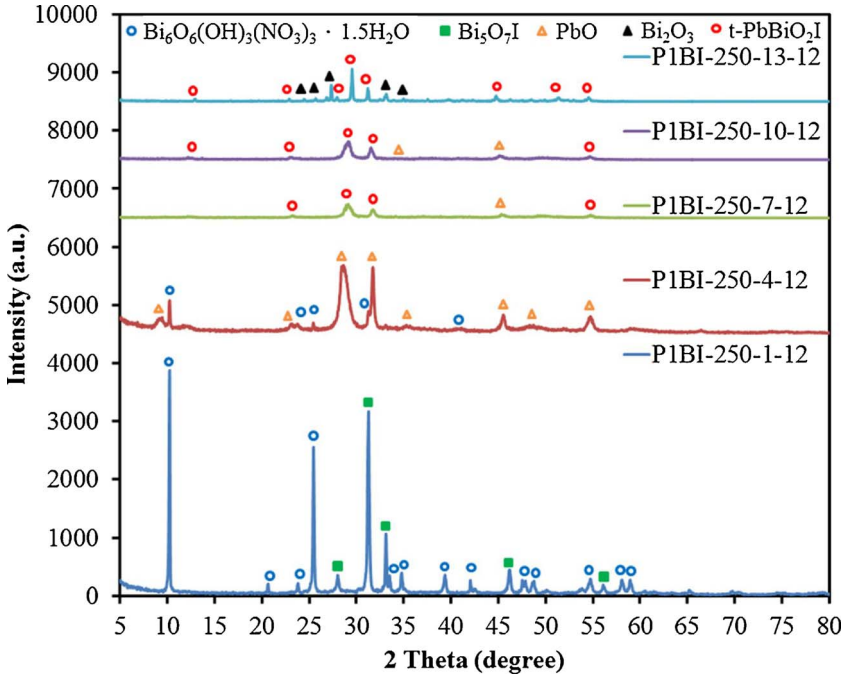

Fig. 1. XRD patterns of as-prepared samples under different pH values, at reaction temperature 250 °C and reaction times 12 h. (Molar ratio $Pb(NO_3)_2$/$Bi(NO_3)_3$ = 1/3).

Table 2
Crystalline phase changes of as-prepared samples under different hydrothermal conditions. ($Pb(NO_3)_2/Bi(NO_3)_3$ = 1/3–3/3, KI = 1 mmol, pH = 1–13, temp = 150–250 °C, time = 12 h). (: Bi_5O_7I : $Bi_6O_6(OH)_3(NO_3)_3{\cdot}1.5H_2O$: PbO : t-$PbBiO_2I$: Bi_2O_3).

Temperature (°C)/Molar ratio (Pb:Bi)	pH value				
	1	4	7	10	13
150(1:3)	■●	■●	■●▲	■▲	○▲
150(3:3)	■●	●▲○	▲○	▲○	▲○
200(1:3)	■●	●▲	▲○	▲○	○▲
200(3:3)	■●	●▲○	●▲○	▲○	▲○
250(1:3)	■●	■●▲	■▲	■▲	○▲
250(3:3)	■●	●▲○	▲○	▲○	■▲

$BiOCl/Bi_6O_6(OH)_3(NO_3)_3{\cdot}1.5H_2O$, t-$PbBiO_2I/Bi_5O_7I$, $PbO/BiOCl/Bi_6O_6(OH)_3(NO_3)_3{\cdot}1.5H_2O/Bi_5O_7I$, $PbO/BiOCl/Bi_6O_6(OH)_3(NO_3)_3{\cdot}1.5H_2O$, and Bi_5O_7I/Bi_2O_3. Table 2 summarizes the results of the XRD measurements. All the as-prepared samples contain t-$PbBiO_2I$ phase (JCPDS 078-0521), PbO phase (JCPDS 085-1287), Bi_5O_7I phase (JCPDS 40-0548), $Bi_6O_6(OH)_3(NO_3)_3{\cdot}1.5H_2O$ phase (JCPDS 053-1038), and Bi_2O_3 (JCPDS 71-0465). In these experiments, pH played a key role, and temperature and molar ratio played a minor role in controlling the composition and anisotropic growth of crystals. From the results of Table 2, the controlled morphology and crystal phase of PbO/t-$PbBiO_2I$ could be completed by simply changing some reaction parameters, including temperature and pH value. $Bi_5O_7I/Bi_6O_6(OH)_3(NO_3)_3{\cdot}1.5H_2O$ was obtained at pH = 1, temp = 150–250 °C, Pb/Bi molar ratio = 3/3–1/3 and pH = 1–4, temp = 150 °C, Pb/Bi molar ratio = 1/3; $Bi_5O_7I/Bi_6O_6(OH)_3(NO_3)_3{\cdot}1.5H_2O/PbO$ was obtained at pH = 7, temp = 150 °C and pH = 4, temp = 250 °C, Pb/Bi molar ratio = 1/3; $Bi_6O_6(OH)_3(NO_3)_3{\cdot}1.5H_2O/PbO/$t-$PbBiO_2I$ was obtained at pH = 4, temp = 150–250 °C, Pb/Bi molar ratio = 3/3 and pH = 4–7, temp = 200 °C, Pb/Bi molar ratio = 3/3; t-$PbBiO_2I/PbO$ was obtained at pH = 7–13, temp = 100 °C, Pb/Bi molar ratio = 3/3 and pH = 7–10, temp = 200 °C, Pb/Bi molar ratio = 3/3 and pH = 10–13, temp = 200 °C, Pb/Bi molar ratio = 3/3 and pH = 10, temp = 250 °C, Pb/Bi molar ratio = 1/3 and pH = 7-10, temp = 250 °C, Pb/Bi molar ratio = 3/3; $Bi_6O_6(OH)_3(NO_3)_3{\cdot}1.5H_2O/PbO$ was obtained at pH = 4, temp = 200 °C, Pb/Bi molar ratio = 1/3; Bi_5O_7I/PbO was obtained at pH = 10, temp = 150 °C, Pb/Bi molar ratio = 1/3 and pH = 7, temp = 250 °C, Pb/Bi molar ratio = 1/3; t-$PbBiO_2I/Bi_2O_3$ was obtained at pH = 13, temp = 150–250 °C, Pb/Bi molar ratio = 1/3; Bi_5O_7I/Bi_2O_3 was obtained at pH = 13, temp = 250 °C, Pb/Bi molar ratio = 3/3. Bi_5O_7I and $Bi_6O_6(OH)_3(NO_3)_3{\cdot}1.5H_2O$ were obtained at higher acidic concentration (pH = 1–4) in the synthetic conditions. Bi_2O_3 microstructures were obtained at higher basic concentration (pH = 13) in the synthetic conditions. t-$PbBiO_2I$ and PbO were obtained at middle concentration (pH = 7–10) in the synthetic conditions.

3.1.2. TEM

Fig. 2 displays that t-$PbBiO_2I/PbO$ is composed of different-size layers, consistent with the TEM observations. In addition, the EDS spectrum shows that the sample contains the elements of Bi, Pb, I, and O. In Fig. 2**(a)**, the HRTEM image demonstrates that two of lattice images are obtained with d-spacing of 0.372 and 0.345 nm, corresponding to the (103) plane of t-$PbBiO_2I$ and the (101) plane of PbO, respectively; it is in strong agreement with the XRD results. The results suggest that the t-$PbBiO_2I/PbO$ phase is formed in the composites, which are favorable for the separation of photoinduced carriers, yielding high photocatalytic efficiency.

3.1.3. Morphological structure and composition

Figs. 3 and **S2** of supplementary data show the FE-SEM images of the composites t-$PbBiO_2I/PbO$, t-$PbBiO_2I/Bi_2O_3$, t-$PbBiO_2I/PbO/BiOCl/Bi_6O_6(OH)_3(NO_3)_3{\cdot}1.5H_2O$,t-$PbBiO_2I/Bi_5O_7I$, $PbO/BiOCl/Bi_6O_6(OH)_3(NO_3)_3{\cdot}1.5H_2O/Bi_5O_7I$, $PbO/BiOCl/Bi_6O_6(OH)_3(NO_3)_3{\cdot}1.5H_2O$, and Bi_5O_7I/Bi_2O_3 at high magnification, respectively. From the observations, the samples show irregular-thick-plate, irregular-nanosheet, and square-plate, thin-square-rod, morphology, respectively. The SEM-EDS results demonstrate that the main elements within such samples are lead, bismuth, oxygen, and iodine, Tables 3 and **S1** of supplementary data. From above results, the composites could be selectively synthesized through a controlled hydrothermal method.

3.1.4. XPS

Fig. 4 presents the Pb 4f, Bi 4f, O 1s, and I 3d XPS spectra of the composites. Observation of the transition peaks involving the Pb 4f, Bi 4f, O 1s, and I 3d orbitals identifies that the catalysts are composed of Bi, Pb, O, and I. From Fig. 4**(a)**, the binding energy 137.0–137.6 and 141.6–142.4 eV is attributed to Pb $4f_{7/2}$ and Pb $4f_{5/2}$ respectively, which could be pointed to Pb at the divalent oxidation state [43]. Logically, because Pb^0 XPS 4f core-levels are occupying much higher binding-energy (BE) region and exhibit another FWHM with a strong asymmetry. Here one can see ~ 0.7 eV shift of the Pb $4f_{7/2\text{-}5/2}$ spin-orbital components towards higher binding energies but, simultaneously, only an essential intensity growth for the ~137 eV and ~141 eV sub-bands (Fig. 4**(a)**). The BE-shift of core-lines to the higher energies region usually is an accepted signature of higher oxidation states for the element in the oxygen-containing compound [44,45]. Kovalev et al. demonstrated that the particle size of PbS could be correlated with observable changes in the binding energy of the Pb XPS peak. They reported that the relative integral intensity of peak depended upon the fraction of particle in the specific region [46], which indicated that higher successive ionic layer adsorption and reaction cycle led to the formation of the fraction of bigger and smaller particles on the surface of titania nanotube. The $4f_{7/2}$ peak observed at 137.8 and 138.9 eV is due to the presence of two different particle sizes of PbS formed in TiO_2 nanotube arrays. The characteristic binding energy value 158.0 eV for Bi $4f_{7/2}$ (Fig. 4**(b)**) shows a trivalent oxidation state for bismuth. A similar chemical binding for Bi $4f_{7/2}$ was also reported by Lee et al. [47]. The asymmetric O 1s peak shown in Fig. 4**(c)** can be split by using the XPS peak-fitting program. The peak at 530.7 eV is assigned to the external −OH group or the water molecule adsorbed on the surface, and the other O 1s peak appearing at 528.7 eV corresponds to lattice oxygen atoms in t-$PbBiO_2I/PbO$ [18,48]. From Fig. 4**(d)**, the binding energy of 618.1–618.8 eV and 629.3–630.2 eV is referred to I $3d_{5/2}$ and I $2p_{3/2}$, respectively, which can be assigned to I at the monovalent oxidation state. These results agree with those of XRD and TEM experiments.

According to earlier studies [47,49], a series of bismuth oxyiodides in the formation process were reported by Chen et al. The proposed processes for the formation of t-$PbBiO_2Cl/PbO$ composites are described in Eqs. (1)–(10). The results demonstrate a series of changes in the compounds prepared at different hydrothermal conditions, described as $PbI_2 \rightarrow Pb(OH)I \rightarrow Pb(OH)_2 \rightarrow PbO$, $BiOCl \rightarrow Bi_4O_5Cl_2 \rightarrow Bi_{24}O_{31}Cl_{10} \rightarrow Bi_3O_4Cl \rightarrow Bi_5O_7Cl \rightarrow Bi_{12}O_{17}Cl_2 \rightarrow Bi_2O_3$, and $BiOI + Pb(OH)_2 \rightarrow PbBiO_2I$ and/or $BiOI + PbO \rightarrow PbBiO_2I$. By controlling the pH of the hydrothermal reaction, different compositions are obtained as follows.

$$Pb^{2+} + 2I^- \rightarrow PbI_{2\ (s)} \quad (1)$$

$$PbI_{2(s)} + OH^- \rightarrow Pb(OH)I_{(s)} \quad (2)$$

$$Pb(OH)I_{(s)} + 2OH^- \rightarrow Pb(OH)_2 \quad (3)$$

$$Pb(OH)_2 \rightarrow PbO_{(s)} + H_2O \quad (4)$$

$$Bi^{3+} + 3OH^- \rightarrow Bi(OH)_{3(s)} \quad (5)$$

$$12Bi(OH)_{3(s)} + 6HNO_3 \rightarrow 2[Bi_6O_6(OH)_3(NO_3)_3{\cdot}1.5H_2O]_{(s)} + 15H_2O \quad (6)$$

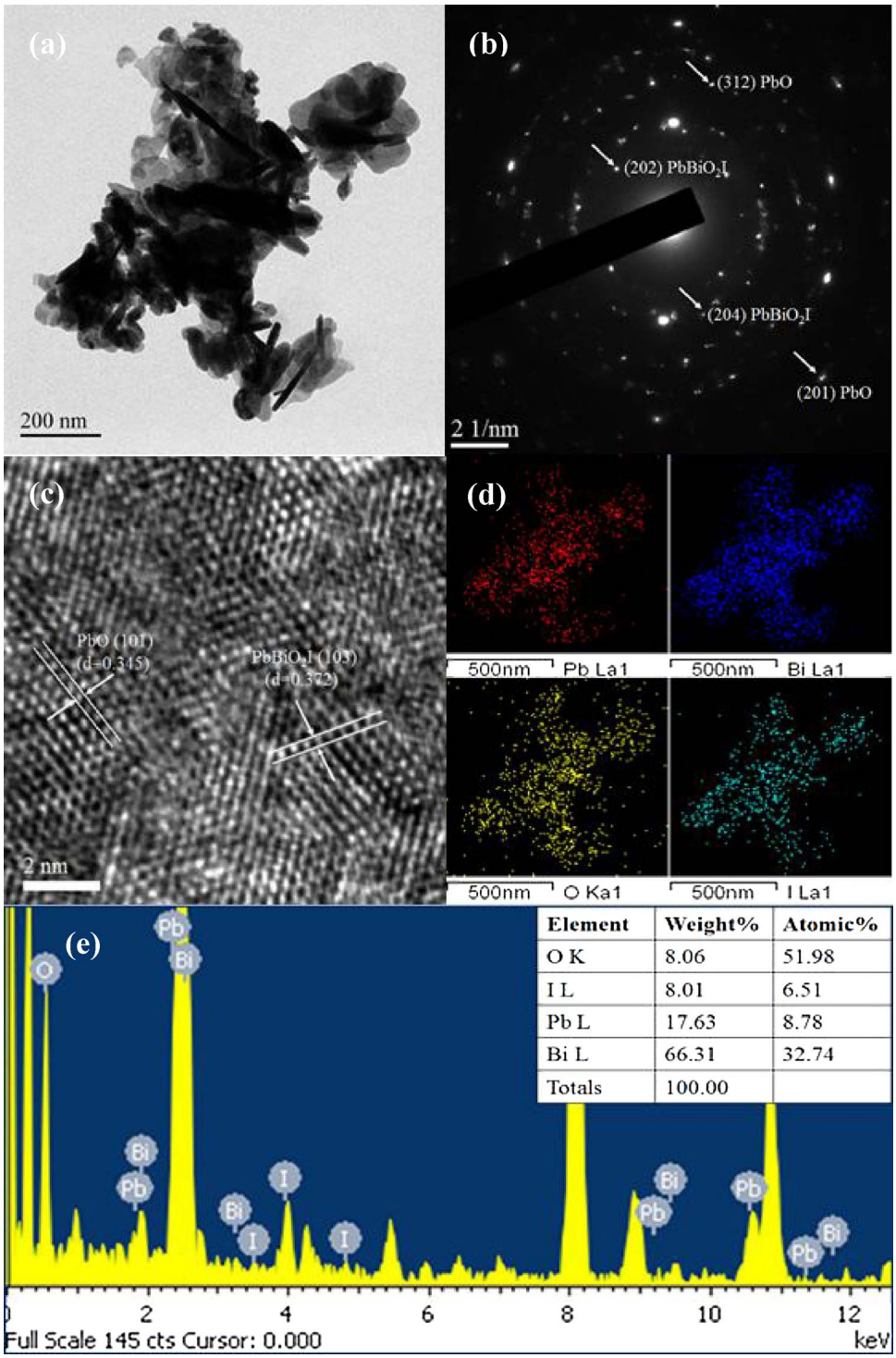

Fig. 2. (a) FE-TEM images, (b) SAD, (c) HR-TEM, (d) mapping, and (e) EDS of *t*-$PbBiO_2I$/PbO (P1BI-250-10-12) sample by the hydrothermal autoclave method.

$$2Bi(OH)_{3(s)} + I^- \rightarrow BiOI_{(s)} + H_2O + OH^- \quad (7)$$

$$Bi^{3+} + 3I^- \rightarrow BiI_{3(s)} \quad (8)$$

$$BiI_{3(s)} + 2OH^- \rightarrow BiOI_{(s)} + 2I^- + H_2O \quad (9)$$

$$BiOI_{(s)} + Pb(OH)_2 \rightarrow PbBiO_2I_{(s)} + H_2O \quad (10)$$

3.1.5. Optical absorption properties

As shown in Figs. 5 and S3 of supplementary data for DR-UV of the as-prepared samples, the absorption edge of the samples is around 518–678 nm, which originates from its band gap of 2.50–3.42 eV and is consistent with the reported results [28,47]. Pure $PbBiO_2I$ and PbO absorb only a small amount of visible light. The E_g value of *t*-$PbBiO_2I$/PbO is determined from a plot of $(\alpha h\nu)^{1/2}$ vs energy ($h\nu$), which is calculated as 2.35 eV.

3.1.6. BET and adsorption-desorption isotherm

From Fig. 6, the samples have S_{BET} around 2.67–12.41 m^2/g. However, the results of Fig. 6 show that the P1BI-250-10-12 (*t*-$PbBiO_2I$/

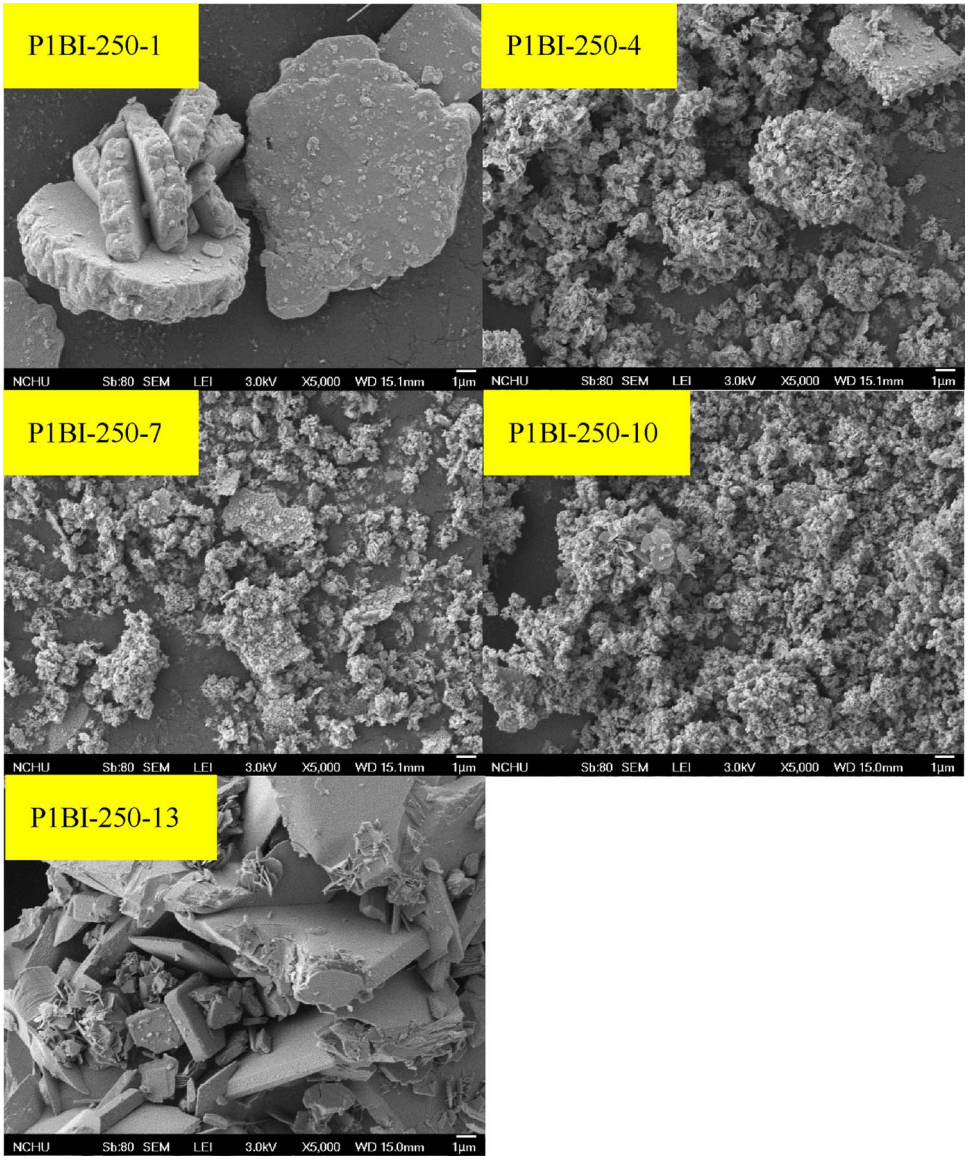

Fig. 3. SEM images of as-prepared samples by the hydrothermal autoclave method at different pH value. (Molar ratio $Pb(NO_3)_2/Bi(NO_3)_3$ = 1/3, temp = 250 °C, time = 12 h).

Table 3
EDS of as-prepared samples prepared under different reaction conditions. ($Pb(NO_3)_2/Bi(NO_3)_3$ = 1/3, KI = 1 mmol, pH = 1–13, temp = 150–250 °C, time = 12 h).

Sample code	EDS of atomic ratio (%)			
	Pb	Bi	O	I
P1BI-150-1	3.60	77.15	19.10	0.16
P1BI-150-4	22.86	55.35	14.58	7.22
P1BI-150-7	18.45	64.39	9.83	7.33
P1BI-150-10	25.21	57.12	12.15	5.51
P1BI-150-13	21.90	49.96	12.30	15.84
P1BI-200-1	0.02	78.99	20.08	0.91
P1BI-200-4	0.84	55.05	8.78	25.33
P1BI-200-7	20.75	42.39	29.98	6.88
P1BI-200-10	23.72	52.20	11.42	8.66
P1BI-200-13	21.98	49.92	12.34	15.76
P1BI-250-1	0.24	82.31	17.45	–
P1BI-250-4	8.53	63.52	17.13	10.81
P1BI-250-7	16.75	56.87	18.40	7.98
P1BI-250-10	17.63	66.31	8.06	8.01
P1BI-250-13	25.88	44.05	13.31	16.75

PbO) sample—which shows the middle S_{BET}—does represent the highest photocatalytic activity ($k = 1.1159 \times 10^{-1}\,h^{-1}$) among the samples, suggesting that the changes in the photocatalytic activity are resulted from *t*-$PbBiO_2I$/PbO composites.

Fig. 6**(a)** shows the nitrogen adsorption-desorption isotherm curves of *t*-$PbBiO_2I$/PbO. The isotherm of *t*-$PbBiO_2I$/PbO is close to Type III without a hysteresis loop at a highly relative pressure between 0.9 and 1.0 [50]. Fig. 6**(b)** shows the corresponding pore-size distribution (PSD) of *t*-$PbBiO_2I$/PbO samples. The mono-modal PSD curve for the samples indicates large macropores (100–2000 nm). Because the nanoplates (or nanosheets) do not contain pores (Fig. 3), the large macropores may reflect porosity within nanoplates (or nanosheets). The large macropores may attribute to the pores formed between stacked nanoplates (or nanosheet), while the large macropores may be ascribed to the pores formed between nanoplates (or nanosheets). Such self-organized porous architectures may be extremely useful in photocatalysis because they provide efficient transport pathways for reactant and product molecules [51]. The pore volume and size of the *t*-$PbBiO_2I$/PbO composite are determined as the pore volume 0.497 cm^3/g and the pore diameter 625.02 nm, respectively.

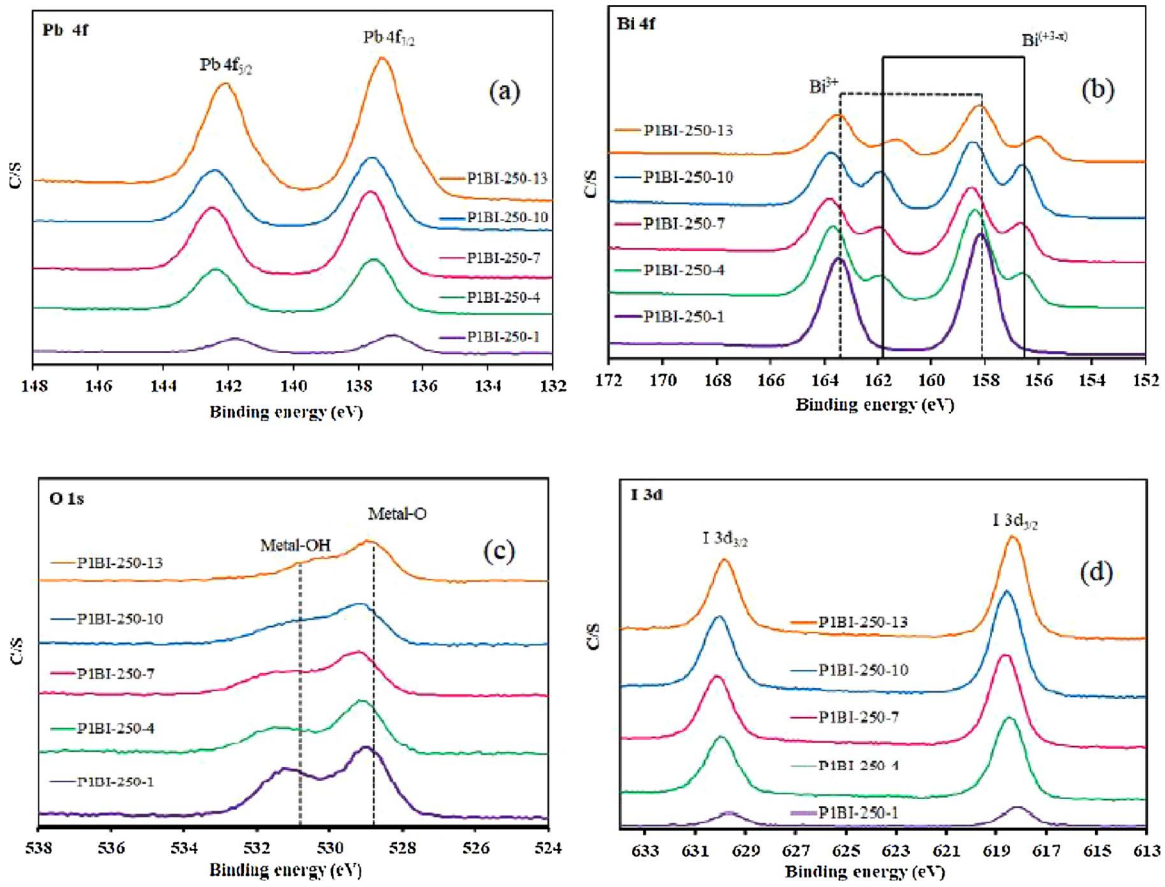

Fig. 4. XPS spectra of as-prepared samples under different pH values, at reaction temperature 250 °C and reaction times 12 h. (Molar ratio $Pb(NO_3)_2/Bi(NO_3)_3$ = 1/3) (a) Pb 4f, (b) Bi 4f, (c) O 1s, (d) I 3d.

3.2. Photocatalytic activity

The changes in the UV–vis spectra during the photodegradation of CV and 2-HBA in aqueous dispersions of *t*-$PbBiO_2I$/PbO composite under visible light irradiation are illustrated in Fig. 7. After visible light irradiation for 72 h, approximately 99.5% of CV and approximately 95% of 2-HBA are decomposed. In Fig. 7**(a)**, the characteristic absorption band of the CV dye at approximately 589.1 nm decreases rapidly with slight hypsochromic shifts (554.7 nm); however, no new absorption band appears even in the ultraviolet range (λ > 200 nm), indicating the possible formation of a series of *N*-de-methylated intermediates and the possible cleavage of the whole conjugated

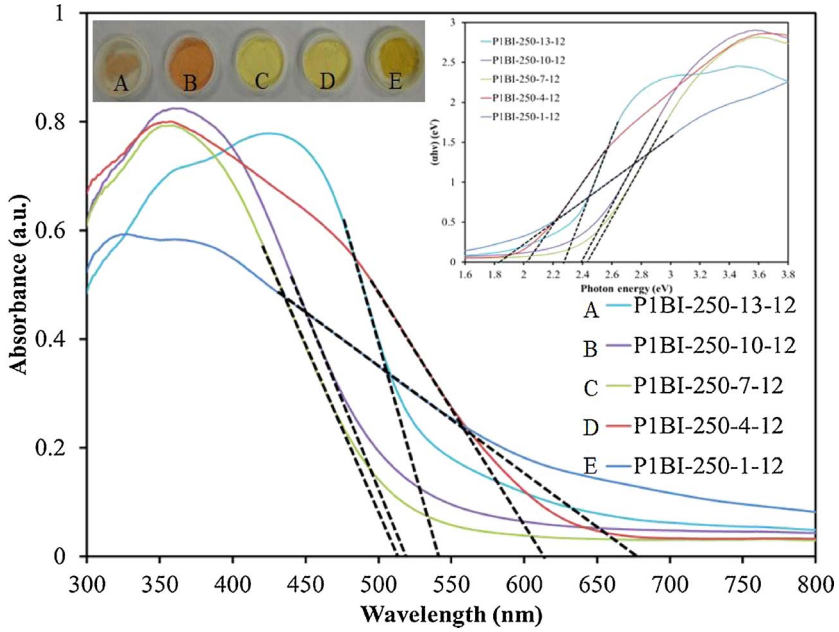

Fig. 5. UV-vis absorption spectra of the as-prepared photocatalysts under different pH values. (Molar ratio $Pb(NO_3)_2/Bi(NO_3)_3$ = 1/3, reaction temp = 250 °C, reaction time 12 h).

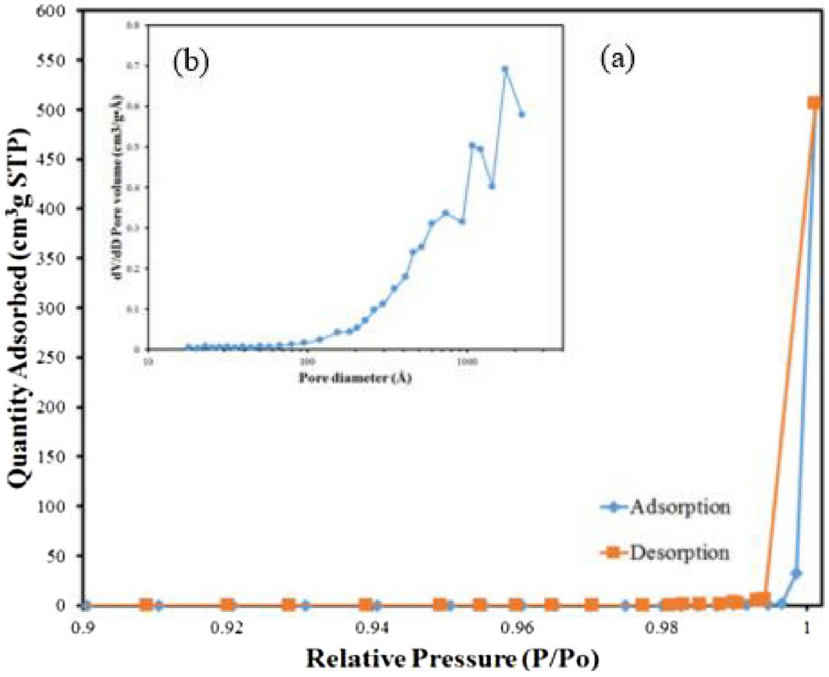

Fig. 6. (a) Nitrogen adsorption-desorption isotherms and (b) the corresponding pore size distribution curve (inset) for *t*-$PbBiO_2I$/PbO.

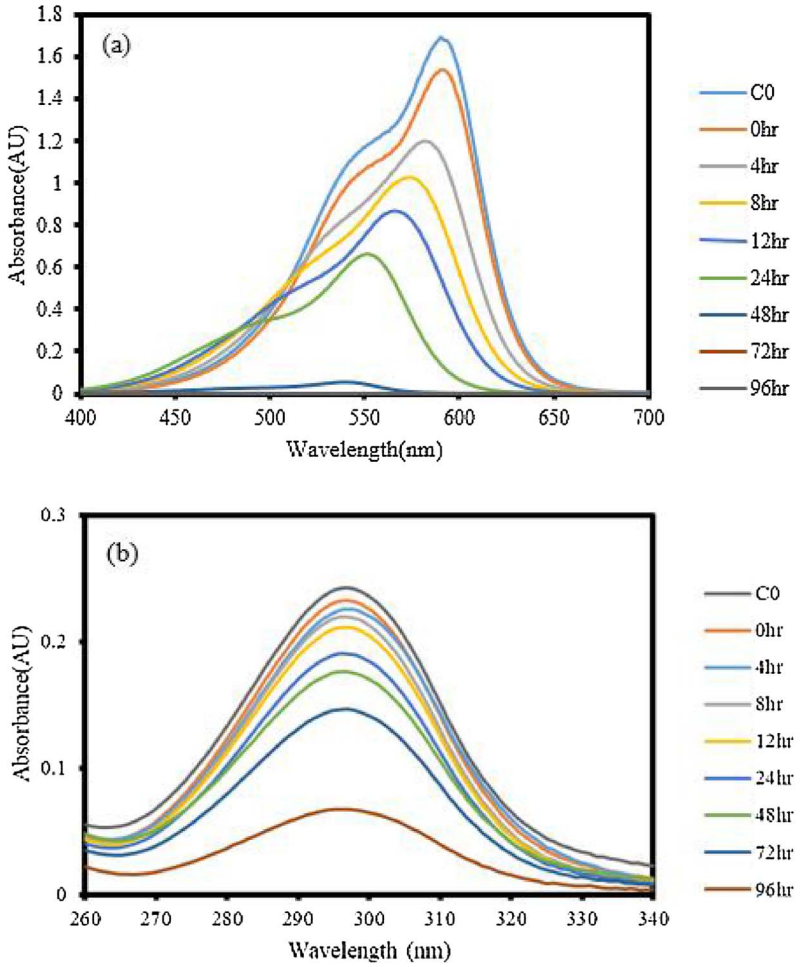

Fig. 7. (a) The photocatalytic degradation of CV over aqueous photocatalyst under visiblelight irradiation l and (b) the photocatalytic degradation of 2-HBA over aqueous photocatalyst under visiblelight irradiation. ((Molar ratio $Pb(NO_3)_2/Bi(NO_3)_3$ = 1/3, pH = 10, reaction temperature = 250°C, reaction time 12 h).

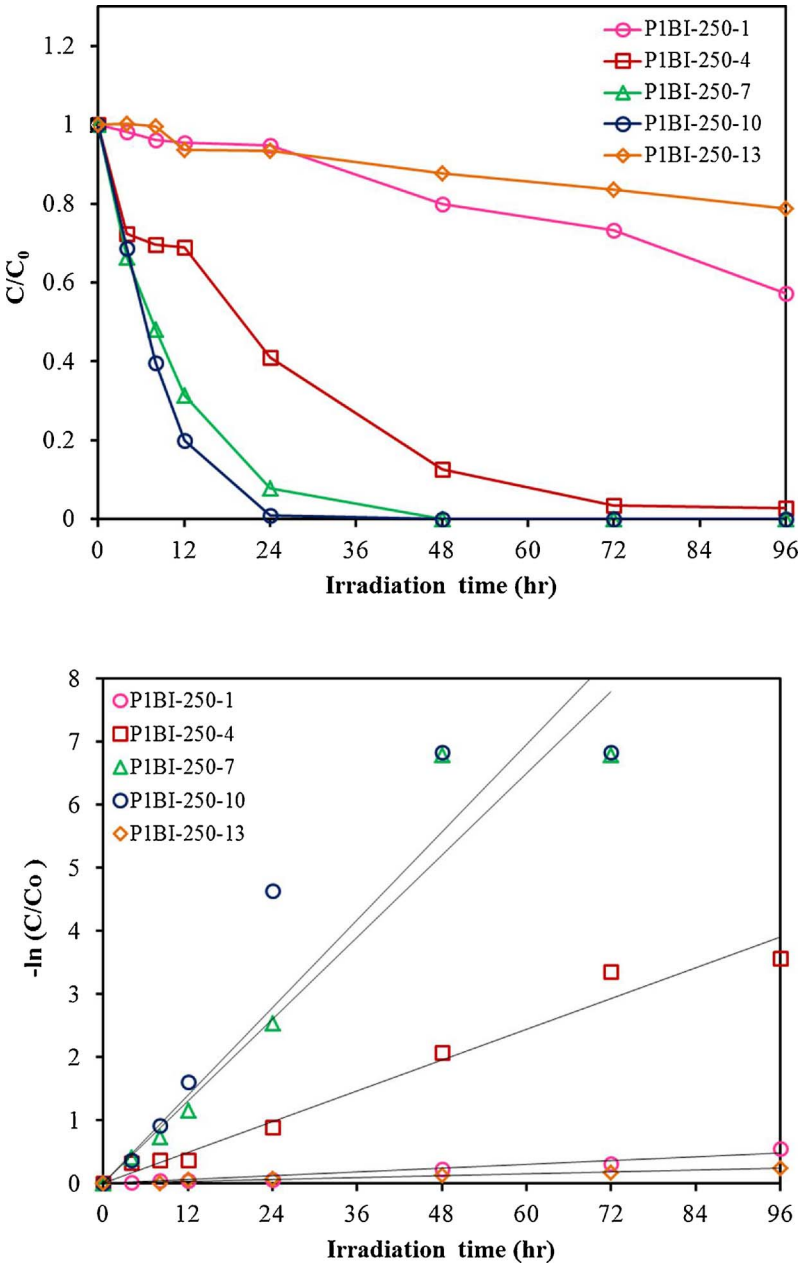

Fig. 8. Photocatalytic degradation of CV as a function of irradiation time over different photocatalysts. (Molar ratio $Pb(NO_3)_2/Bi(NO_3)_3$ = 1/3, pH = 1–13, reaction temperature = 250°C, reaction time 12 h).

chromophore structure of the CV dye. Further irradiation causes the absorption band at 554.7 nm to decrease; however, no further wavelength shift is observed, suggesting that the band at 554.7 nm is that of the full *N*-de-methylated product of the CV dye [8,9].

The degradation efficiency as a function of reaction time is illustrated in Figs. 8 and S4 of supplementary data; the removal efficiency is significantly enhanced in the presence of the as-prepared samples. After the irradiation for 24 h, *t*-$PbBiO_2I$/PbO exhibits a superior photocatalytic performance, with the CV removal efficiency up to 99%. To further understand the reaction kinetics of CV degradation, the apparent pseudo-first-order model [52] expressed by the equation of ln (C_o/C) = kt is applied in the experiments. Via the first-order linear fit of the data shown in Table 4, the k value of *t*-$PbBiO_2I$/PbO is obtained as the maximum degradation rate of $1.159 \times 10^{-1}\ h^{-1}$, which is much higher than that of the other composites; the *t*-$PbBiO_2I$/PbO composite is a much more effective photocatalyst than the others synthesized in this study.

It can be assumed that the enhanced photocatalytic activities of composites could be ascribed to a synergistic effect, including high BET surface area, the formation of the heterojunction, layered structure, and low energy band structure. To investigate the BET surface area in the heterostructures, the BET surface areas of *t*-$PbBiO_2I$/PbO samples are measured. The lower BET surface areas of *t*-$PbBiO_2I$/PbO composites suggest the lower photocatalytic activity. As is known, the photocatalysts are excited to generate electron–hole pairs directly after the illumination in the photocatalytic process. Moreover, the photocatalytic efficiency mainly depends on the recombination rate or the lifetime of the photogenerated electron–hole pairs. The faster recombination occurs, the less time is required for the chemical reactions. Therefore, PL spectra are utilized for investigating the recombination rate of the photogenerated electron–hole pairs [53]. To investigate the separation capacity of the photogenerated carriers in the heterostructures, the PL spectra of *t*-$PbBiO_2I$/PbO, *t*-$PbBiO_2I$, and PbO

Table 4
Pseudo-first-order rate constant for CV photocatalytic oxidation under different photocatalysts.

Photocatalyst	k (h^{-1})	R^2	Photocatalyst	k (h^{-1})	R^2
P3BI-150-1	0.0037	0.9243	P1BI-150-1	0.0024	0.884
P3BI-150-4	0.0987	0.8644	P1BI-150-4	0.0076	0.9559
P3BI-150-7	0.0597	0.9972	P1BI-150-7	0.0538	0.9509
P3BI-150-10	0.0391	0.9131	P1BI-150-10	0.0534	0.943
P3BI-150-13	0.0221	0.8869	P1BI-150-13	0.0061	0.9472
P3BI-200-1	0.0036	0.9272	P1BI-200-1	0.0109	0.8313
P3BI-200-4	0.0575	0.9900	P1BI-200-4	0.1068	0.9588
P3BI-200-7	0.0649	0.9586	P1BI-200-7	0.0600	0.9615
P3BI-200-10	0.0038	0.9577	P1BI-200-10	0.0714	0.8799
P3BI-200-13	0.0306	0.8944	P1BI-200-13	0.0716	0.9299
P3BI-250-1	0.002	0.9318	P1BI-250-1	0.0051	0.9511
P3BI-250-4	0.0501	0.9444	P1BI-250-4	0.0407	0.9752
P3BI-250-7	0.0445	0.9615	P1BI-250-7	0.1082	0.9313
P3BI-250-10	0.0155	0.9598	P1BI-250-10	0.1159	0.8635
P3BI-250-13	0.0251	0.882	P1BI-250-13	0.0025	0.9677

samples are measured; the results are shown in Fig. 9. A weak emission peak around 440–540 nm appears for the as-prepared samples, which could have been derived from the direct electron–hole recombination of band transitions. However, the characteristic emission peak around the lowest intensity 470 nm for *t*-$PbBiO_2I$/PbO indicates that the recombination of photogenerated charge carriers is greatly inhibited. The efficient separation of charge could increase the lifetime of charge carriers and enhance the efficiency of interfacial charge transfer to the adsorbed substrates, thus improving the photocatalytic activity. The comparison of rate constant by different photocatalysts is shown in Table 4. The order of rate constant presents *t*-$PbBiO_2I$/PbO, k = 0.1159 > Bi_5O_7I/PbO, k = 0.1082 > $BiOCl/Bi_6O_6(OH)_3(NO_3)_3{\cdot}1.5H_2O$/PbO, k = 0.1068 > *t*-$PbBiO_2I$, k = 0.0358 > PbO, k = 0.010. The photocatalytic activity of the *t*-$PbBiO_2I$/PbO composite reaches the maximum rate constant of 0.1159 h^{-1}, 3 times higher than that of *t*-$PbBiO_2I$ and 20 times higher than that of PbO. Thus, the *t*-$PbBiO_2I$/PbO composite may also play a role in the enhancement of photocatalytic activity.

The durability of *t*-$PbBiO_2I$/PbO is evaluated by recycling the used catalyst. After each cycle, the catalyst is collected by centrifugation. No apparent loss is observed in the photocatalytic activity when CV is removed in the 3rd cycle; even during the sixth run, the decline in the photocatalytic activity is 9% (Fig. 10**(a)**). The used *t*-$PbBiO_2I$/PbO is also examined by XRD, and no detectable difference is observed between the as-prepared and the used samples (Fig. 10**(b)**); hence, *t*-$PbBiO_2I$/PbO has good photostability.

Photocatalytic activity of PbO was measured, which has a layered structure similar to the polycationic sheets [$PbBiO_2^+$] in the title compound, did not demonstrate any catalytic activity at all, although the absorption spectrum was quite similar. Hence, photocatalytic activity due to Pb^{2+} can be ruled out. Earlier report [27] has discussed mainly electronic reasons for the different photocatalytic activity of layered ABO_2X-type materials (A = Pb; B = Bi, Sb; X = Cl, Br, I) [30,32,36,37,54,55]. Nevertheless, crystal-chemical arguments should also be taken into consideration to explain the catalytic property of the compound. A possible explanation for the different photocatalytic activity of the bi-metal-oxides may be obtained collectively from their crystal structures, optical and redox properties. All the solid materials under discussion crystallize in a layered structure. They show co-valent metal oxide layer [$PbBiO_2^+$] separated by halide layer, which are stacked along [001]. One can suppose that the crystal surface be compose of metal oxide layers, i.e., the metal atoms are thought to form the (001) surfaces [27]. It is likely that Bi^{3+} is responsible for the catalytic properties by visible-light irradiation in this system.

Surprisingly, Pfitzner et al. described that only $PbBiO_2X$ where X = Cl and Br catalyzed the photo-reduction of nitrobenzene to aniline, while no conversion happened for $PbBiO_2I$ when irradiated under comparable conditions. Furthermore, the latter materials absorb a significant part of the visible-light spectrum [22]. The experimentally determined optical band gaps were 2.55 eV ($PbBiO_2Cl$), 2.47 eV ($PbBiO_2Br$) and 2.39 eV ($PbBiO_2I$) [54]. It seems that the band gaps of all these semiconductors are in the right range to catalyze the observed reaction. Hence, changes in the structural nature of the materials may be determinative; increasing the iodine content in $PbBiO_2X$ leads to a change of the preferred crystal growth directions. Thus, $PbBiO_2Cl$ and $PbBiO_2Br$ form layered crystals along (001), whereas $PbBiO_2I$ crystal-

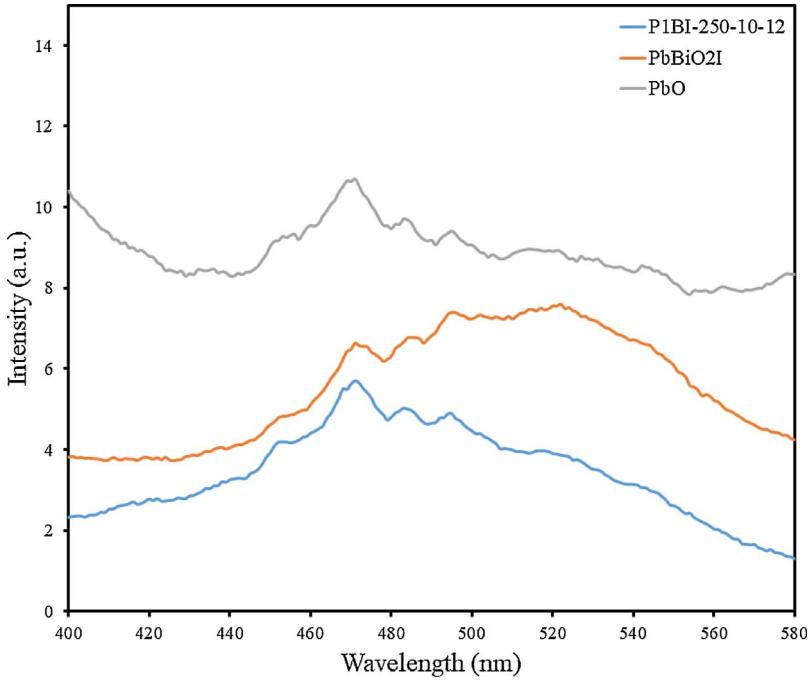

Fig. 9. Photoluminescence (PL) spectra of the as-prepared photocatalysts.

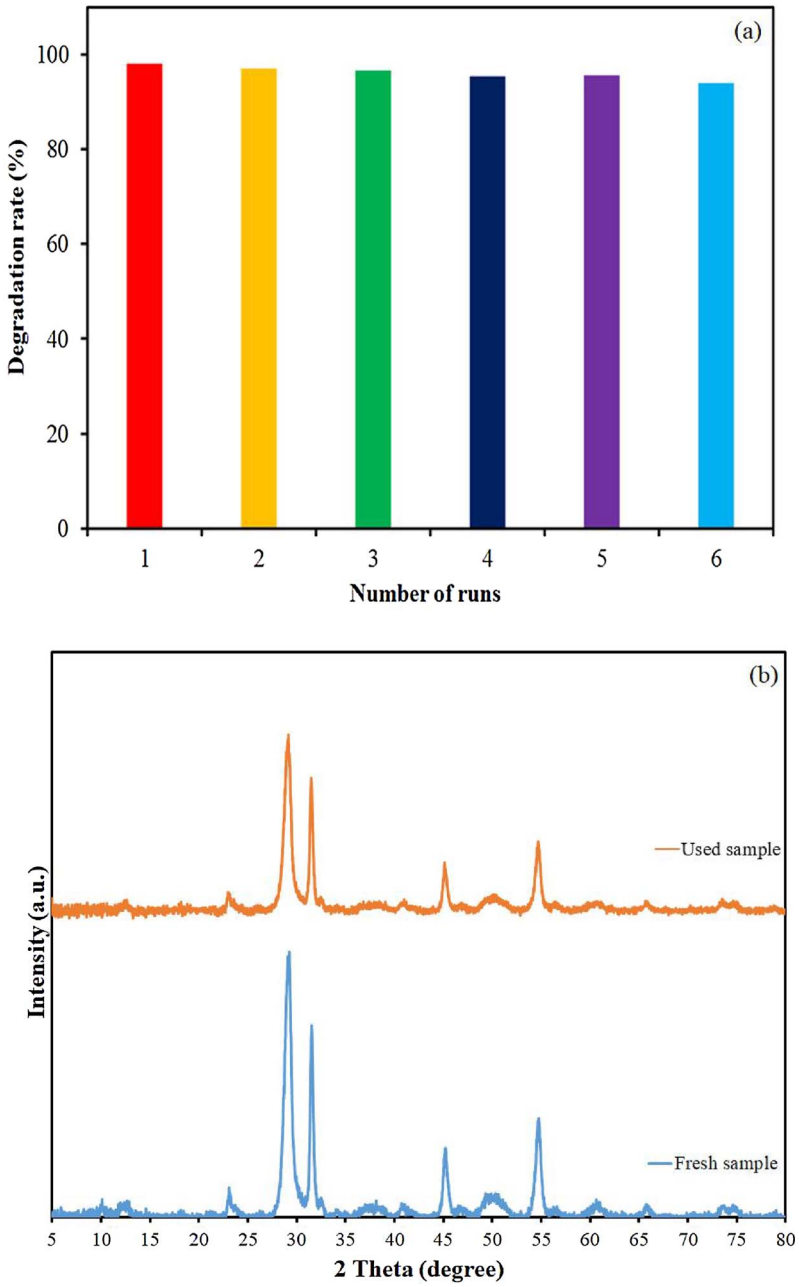

Fig. 10. (a) Cycling runs and (b) XRD patterns acquired before and after in the pho-tocatalytic degradation of CV in the presence of P1BI-250-10-12 (*t*-$PbBiO_2I$/PbO).

lizes as rods with [001] as the rod axis. Changes in the bonding interactions between the halide and metal atoms indicate this clearly. In the case of rod-like crystals, the surface of the material is significantly different; the surfaces change from mainly (001) for chloride and bromide to mainly (100) and (010) for iodide, which may alter the photocatalytic activities. The stronger bonds of iodine to Pb or Bi, well known for the binary metal halides, change the crystal growth and may de-activate the surfaces. Furthermore, redox quenching by iodine may intercept the photocatalysis as well. Accordingly, the redox potentials of the oxide halides were measured, showing multiple redox processes that did not permit the derivation of exact values [56]. Although, iodide in activation has been researched with the semiconductors $PbBiO_2Br_nI_m$ and $PbBiO_2Cl_nI_m$ with varying ratios of their halogen content and analyses of their catalytic activities in nitrobenzene reduction. With an increasing content of iodine in $PbBiO_2Br_nI_m$ and $PbBiO_2Cl_nI_m$, the photocatalytic efficiencies decreased dramatically [27].

3.3. Photodegradation mechanism of CV

In general, three possible reaction pathways are assumed to be involved in the photodegradation of organic compounds by a photocatalyst, includingphotocatalysis, photolysis, and dye photosensitization [57]. In the photolysis process, a photoinduced electron on the induced organism directly reacts with O_2 to produce a $^1O_2$ that acts as an oxidant for the photolysis of organism [58]. In the experiments, CV degradation induced by photolysis under visible light in a blank experiment is not observable, CV is a structure-stable dye, and the decomposition by the photolysis mechanism is negligible.

As people may know, various primary active species, such as HO·, h^+, O_2^-·, H· and $^1O_2$, could be generated during the photocatalytic degradation reaction in UV-vis/semiconductor systems [58,59]. Dimitrijevic et al. [59] proposed the three-fold role of water, both dissociated on the surface of TiO_2 and in subsequent molecular layers, as (i) the stabilization of charges, preventing electron-hole recombination,

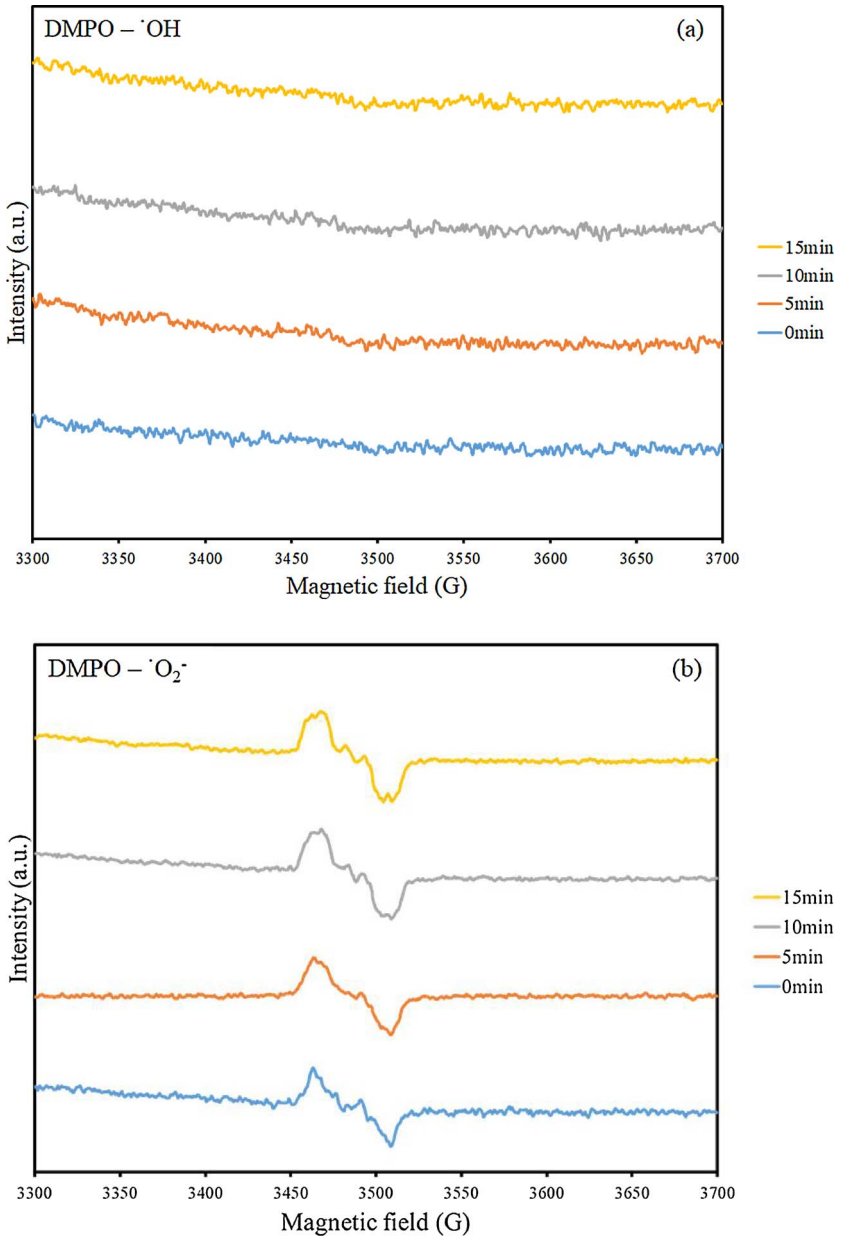

Fig. 11. DMPO spin-trapping EPR spectra for (a) DMPO-OH and (b) DMPO-O_2^- under visible light irradiation with P1BI-250-10 (*t*-$PbBiO_2I$/PbO).

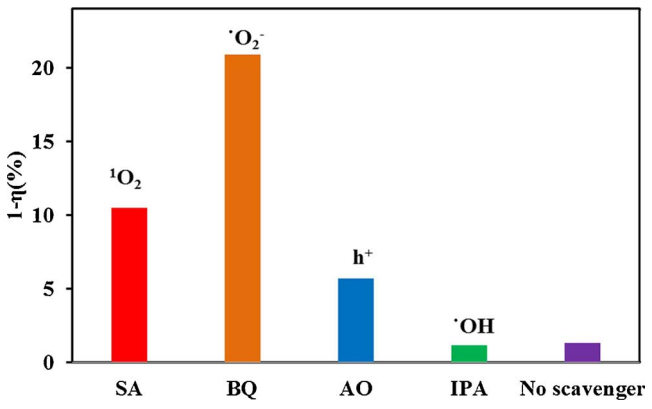

Fig. 12. Photodegradation of CV dye (*t*-$PbBiO_2I$/PbO) in the presence of different scavengers under solar light irradiation.

(ii) an electron acceptor, the formation of H atoms in a reaction of photo-generated electrons with protons on the surface, $-OH_2^+$, and (iii) an electron donor, the reaction of water with photo-generated holes to give ·OH radicals. Ma et al. revealed that O_2^-· was the main active species for NO oxidation to NO_3^- with TO_2/g-C_3N_4 under visible and UV light [60]. Zou's group illustrated a typical Cu_2O–reduced graphene oxide photocatalyst favorable for the production of O_2^-· reactive species for methylene blue [61]. Jiang et al. revealed that the photo-generated h^+ and O_2^-· were the main oxidative species for the degradation of methyl orange [62]. The generation of O_2^-· could not only inhibit the recombination of photoinduced charge carriers but also benefit the de-chlorination of chlorinated phenol derivative. The hydroxyl radical HO· might only be formatted via an $e^- \rightarrow O_2^-$· → H_2O_2 → ·OH route. Meanwhile, ·OH radicals are formatted by multi-step O_2^-· reduction in the system [63]. Kondrakov et al. reported the study on the photocatalytic generation of free OH radicals (·OH_{free}) in aqueous TiO_2 suspensions using an ^{18}O isotope labeling and a "remote" photocatalysis approach. A probe compound, 1,3,5-trichlorobenzene (TCB), was adsorbed in pores of silica gel (SG) microparticles to be

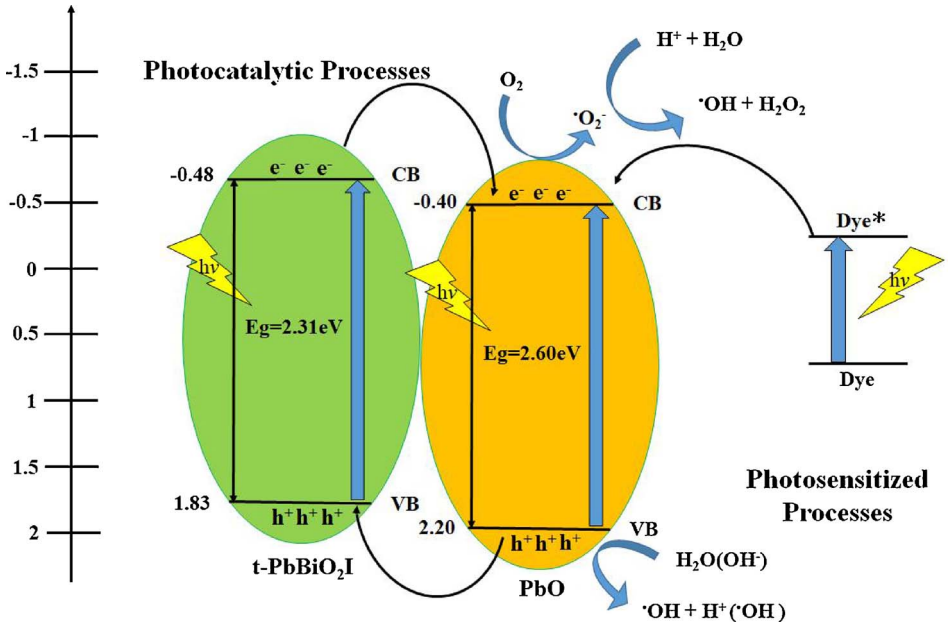

Fig. 13. Schematic illustration of the band gap structures of *t*-$PbBiO_2I$/PbO.

shielded from the direct hole oxidation [64]. According to earlier studies [61], the photocatalytic process was mainly governed by $O_2^-\cdot$, rather than by ·OH, e^- or h^+. In earlier study, CV photodegradation by BiO_mX_n/BiO_pX_q (X, Y = Cl, Br, I) under visible light was dominated by $O_2^-\cdot$ oxidation being the main active species and ·OH and h^+ being the minor active species [63,65]. Lin et al. reported that $O_2^-\cdot$ and ·OH were the two main actives in the photocatalytic degradation process of CV dye using $PbBiO_2Br$/BiOBr [10]. Liu et al. reported that $O_2^-\cdot$, $^1O_2$, ·OH, and h^+ were the main actives in the photocatalytic degradation process of CV dye using $PbBiO_2Cl$/BiOCl [38]. On the basis of the references presented above, it is proposed that the probability of forming ·OH should be much lower than that for $O_2^-\cdot$; however, ·OH is an extremely strong and nonselective oxidant, which leads to the partial or complete mineralization of several organic chemicals.

In order to evaluate the effect of the active species during the photocatalytic reaction, EPR measurement is used for scavenging the relevant active species. From Fig. 11, only are the characteristic peaks of DMPO−$O_2^-\cdot$ adducts observed under visible light irradiated *t*-$PbBiO_2I$/PbO suspension. Fig. 11**(a)** shows that no EPR signal is observed and Fig. 11**(b)** shows that EPR signals ($^1O_2$) are observed when the reaction is performed in the dark, while the signals with the intensity corresponding to the characteristic peak of DMPO−$O_2^-\cdot$ adducts [66] are observed during the reaction process under visible light irradiation, and the intensity gradually increases with the prolonged reaction time. It suggests that O_2^- and $^1O_2$ being active species are formed in the presence of *t*-$PbBiO_2I$/PbO and oxygen under visible light irradiation.

In order to re-evaluate the effect of the active species during the photocatalytic reaction, different quenchers are used for scavenging the relevant active species. As shown in Fig. 12, the photocatalytic degradation of CV is obviously affected by the addition of SA, AO, and BQ, and IPA quenching decreases evidently compared with that of no-quenching, indicating that $O_2\cdot^-$, $^1O_2$, and h^+ are the active species in the mechanism of photocatalytic degradation of CV. Hence, the quenching effects of scavengers and EPR illustrate that the reactives $O_2\cdot^-$ and $^1O_2$ play the major role and h^+ plays the minor role in the photocatalytic degradation of CV. The generation of $O_2^-\cdot$ could not only inhibit the recombination of photoinduced charge carriers but also benefit the degradation of CV. $O_2^-\cdot$ might be formatted by an e^- with O_2 and/or $^1O_2$ with e^- species. Fig. 13 shows the band alignment derived for a type-II heterostructure [67] and VBM XPS spectra derived for *t*-$PbBiO_2I$ and PbO. The CBM and VBM positions measured for the *t*-$PbBiO_2I$ semiconductor were presened to be higher than those determined for the PbO semiconductors. The VBM edge noted for *t*-$PbBiO_2I$ was at approximately 1.83 eV, concordant with the position noted by Fuldner et al. [27]. Regarding PbO, the derived VBM edges were at 2.20 eV. For that reason, band potentials derived for *t*-$PbBiO_2I$ and PbO are illustrated to be suitable. The photo-induced electrons occurring on the surface of *t*-$PbBiO_2I$ could be delivered conveniently to PbO, all occurring through the interfaces; similarly, the holes existing on the surface of PbO could deliver to *t*-$PbBiO_2I$. The observed charge transfer was thus noted to be effective in hindering electron–hole recombination in the two semiconductors, consequently causing photocatalytic efficiency improvement. Once the electron and the hole reach the CB and the VB of *t*-$PbBiO_2I$/PbO, the formation of active oxygen species, which cause the degradation of CV, would be induced. It is clear that, except for the photodegradation of CV by the route of *t*-$PbBiO_2I$/PbO-mediated and photosensitized processes, another type of photocatalytic route accounts for the enhanced photocatalytic activity. In Fig. 13, both the photosensitized and photocatalytic processes are preceded concurrently. However, in photosensitized and photocatalytic processes, O_2^- radicals are generated by the reaction of photogenerated and photosensitized electrons with oxygen gas on the photocatalyst surface, and $^1O_2$ is also generated by the reaction of O_2 radicals with photocatalyst. These cycles continuously occur when the system is exposed to visible-light irradiation [63]; and, after several cycles of photo-oxidation, the degradation of CV by the produced oxidant species can be expressed by Eqs. (11) and (12).

$$CV + O_2^-\cdot/^1O_2/h^+ \rightarrow \text{degraded compounds} \quad (11)$$

$$CV^+\cdot + O_2^-\cdot/^1O_2/h^+ \rightarrow \text{degraded compounds} \quad (12)$$

The reaction mechanisms for *t*-$PbBiO_2I$/PbO-mediated photocatalytic processes proposed in this research should offer some notions for the applications to the decoloration of dyes.

4. Conclusions

The *t*-$PbBiO_2I$/PbO composites have been synthesized by using template-free hydrothermal methods for the first time. The removal efficiency is significantly enhanced in the presence of *t*-$PbBiO_2I$/PbO composites. The increased photocatalytic activities of *t*-$PbBiO_2I$/PbO

composites could be attributed to the formation of the heterojunction between $PbBiO_2I$ and PbO, which effectively suppresses the recombination of photo-generated electron–hole pairs. The quenching effects of scavengers and EPR illustrate that the reactive $O_2\cdot^-$ and $^1O_2$ play the major role, and h^+ plays the minor role in the photocatalytic degradation of CV and 2-HBA. This work is useful for the synthesis of *t*-$PbBiO_2I$/PbO and the photocatalytic degradation of CV as well as 2-BHA in future applications to environmental pollution and control.

Acknowledgment

This research was supported by the Ministry of Science and Technology of the Republic of China (MOST-106-2113-M-142 −001).

Appendix A. Supplementary data

Supplementary data associated with this article can be found, in the online version, at https://doi.org/10.1016/j.cattod.2018.02.006.

References

[1] M.R. Hoffmann, S.T. Martin, W. Choi, D.W. Bahnemann, Chem. Rev. 95 (1995) 69–96.
[2] M. Urbani, M. Grätzel, M.K. Nazeeruddin, T. Torres, Chem. Rev. 114 (2014) 12330–12396.
[3] A. Kubacka, M. Fernández-García, G. Colón, Chem. Rev. 112 (2012) 1555–1614.
[4] D.F. Duxbury, Chem. Rev. 93 (1993) 381–433.
[5] B.P. Cho, T. Yang, L.R. Blankenship, J.D. Moody, M. Churchwell, F.A. Bebland, S.J. Culp, Chem. Res. Toxicol. 16 (2003) 285–294.
[6] S.Y. Chou, C.C. Chen, L.W. Chen, Y.M. Dai, J.H. Lin, W.W. Lee, RSC Adv. 6 (2016) 33478–33491.
[7] S.Y. Chou, W.H. Chung, L.W. Chen, Y.M. Dai, W.Y. Lin, J.H. Lin, C.C. Chen, RSC Adv. 6 (2016) 82743–82758.
[8] H.P. Lin, C.C. Chen, W.W. Lee, Y.Y. Lai, J.Y. Chen, Y.Q. Chen, J.Y. Fu, RSC Adv. 6 (2016) 2323–2336.
[9] S.T. Huang, Y.R. Jiang, S.Y. Chou, Y.M. Dai, C.C. Chen, J. Mol. Catal. A: Chem. 391 (2014) 105–120.
[10] H.P. Lin, W.W. Lee, S.T. Huang, L.W. Chen, T.W. Yeh, J.Y. Fu, C.C. Chen, J. Mol. Catal. A: Chem. 417 (2016) 168–183.
[11] K. Yu, S. Yang, C. Liu, H. Chen, H. Li, C. Sun, S.A. Boyd, Environ. Sci. Technol. 46 (2012) 7318–7326.
[12] W.L.W. Lee, J.S. Lin, J.L. Chang, J.Y. Chen, M.C. Cheng, C.C. Chen, J. Mol. Catal. A: Chem. 361–362 (2012) 80–90.
[13] Y. He, H. Huang, Y. Zhang, X. Li, N. Tian, Y. Guo, Y. Luo, Mater. Res. Bull. 64 (2015) 405–409.
[14] D.O. Charkin, P.S. Berdonosov, V.A. Dolgikh, P. Lightfoot, J. Solid State Chem. 175 (2003) 316–321.
[15] A.M. Kusainova, P. Lightfoot, W. Zhou, Chem. Mater. 13 (2001) 4731–4737.
[16] H. Cheng, B. Huang, Y. Dai, Nanoscale 6 (2014) 2009–2026.
[17] L. Ye, J. Chen, L. Tian, J. Liu, T. Penga, K. Deng, L. Zan, Appl. Catal. B: Environ. 130–131 (2013) 1–7.
[18] Y.R. Jiang, H.P. Lin, W.H. Chung, Y.M. Dai, W.Y. Lin, C.C. Chen, J. Hazard. Mater. 283 (2015) 787–805.
[19] Y.H. Liao, J.X. Wang, J.S. Lin, W.H. Chung, W.Y. Lin, C.C. Chen, Catal.Today 174 (2011) 148–159.
[20] Z. Chen, H. Jiang, W. Jin, C. Shi, Appl. Catal. B: Environ. 180 (2016) 698–706.
[21] J.A. Seabold, K.S. Choi, J. Am. Chem. Soc. 134 (2012) 2186–2192.
[22] W. Wei, Y. Dai, B.B. Huang, J. Phys. Chem. C 113 (2009) 5658–5663.
[23] M. Batuk, D. Batuk, A.A. Tsirlin, D.S. Filimonov, Chem. Mater. 27 (2015) 2946–2956.
[24] J.F. Ackerman, Mat. Res. Bull. 17 (1982) 883–886.
[25] F.J. Maile, G. Pfaff, P. Reynders, Prog. Org. Coat. 54 (2005) 150.
[26] J. Ketterer, V. Kramer, Mat. Res. Bull. 20 (1985) 1031–1036.
[27] S. Füldner, P. Pohla, H. Bartling, S. Dankesreiter, R. Stadler, M. Gruber, A. Pfitzner, B. König, Green Chem. 13 (2011) 640–643.
[28] F.Y. Xiao, J. Xing, L. Wu, Z.P. Chen, X.L. Wang, H.G. Yang, RSC Adv. 3 (2013) 10687–10690.
[29] Y. Yu, Y. Gu, W. Zheng, Y. Ding, Y. Cao, J. Phys. Chem. C 119 (2015) 28190–28193.
[30] Z. Shan, W. Wang, X. Lin, H. Ding, F. Huang, J. Solid State Chem. 181 (2008) 1361–1366.
[31] S. Rau, B. Schäfer, D. Gleich, E. Anders, M. Rudolph, M. Friedrich, H. Görls, W. Henry, J.G. Vos, Angew. Chem. 118 (2006) 6361–6364.
[32] A. Pfitzner, P. Pohla, Z. Anorg. Allg. Chem. 635 (2009) 1157–1159.
[33] D.O. Charkin, O.S. Morozov, E.A. Ul'Yanova, P.S. Berdonosov, V.A. Dolgikh, C. Dickinson, W. Zhou, P. Lightfoot, Solid State Sci. 8 (2006) 1029–1034.
[34] B. Wang, J. Di, P. Zhang, J. Xia, S. Dai, H. Li, Appl. Catal. B: Environ. 206 (2017) 127–135.
[35] B. Wang, J. Di, G. Liu, S. Yin, J. Xia, Q. Zhang, H. Li, J. Colloid Interface Sci. 507 (2017) 310–322.
[36] Z. Shan, X. Lin, M. Liu, H. Ding, F. Huang, Solid State Sci. 11 (2009) 1163–1169.
[37] S. Yin, T. Wu, M. Li, J. Di, M. Ji, B. Wang, Y. Chen, J. Xia, H. Li, CrystEngComm 19 (2017) 4777–4788.
[38] F.Y. Liu, Y.R. Jiang, C.C. Chen, W.W. Lee, Catal. Today 300 (2018) 112–123.
[39] X. Li, J. Wang, D. Xu, Z. Sun, Q. Zhao, W. Peng, Y. Li, G. Zhang, F. Zhang, X. Fan, ACS Sustain. Chem. Eng. 3 (2015) 1017–1022.
[40] M.C. Yin, Z.S. Li, J.H. Kou, Z.G. Zou, Environ. Sci. Technol. 43 (2009) 8361–8366.
[41] G. Li, K.H. Wong, X. Zhang, C. Hu, J.C. Yu, R.C.Y. Chan, P.K. Wong, Chemosphere 76 (2009) 1185–1191.
[42] S.G. Meng, D.Z. Li, M. Sun, W.J. Li, J.X. Wang, J. Chen, X.Z. Fu, G.C. Xiao, Catal. Commun. 12 (2011) 972–975.
[43] M.M. Rahman, K.M. Krishna, T. Soga, T. Jimbo, M. Umeno, J. Phys. Chem. Solid 60 (1999) 201–210.
[44] D.A. Zatsepin, D.W. Boukhvalov, N.V. Gavrilov, A.F. Zatsepin, V.Ya. Shur, A.A. Esin, S.S. Kim, E.Z. Kurmaev, Appl. Surf. Sci. 400 (2017) 110–117.
[45] D.A. Zatsepin, D.W. Boukhvalov, N.V. Gavrilov, E.Z. Kurmaev, A.F. Zatsepin, L. Cuif, V. Ya Shur, A.A. Esin, Appl. Surf. Sci. 405 (2017) 129–136.
[46] A.I. Kovalev, D.L. Wainstein, A.Y. Rashkovskiy, A. Osherov, Y. Golan, Surf. Interface Anal. 42 (2010) 850–854.
[47] Y.H. Lee, Y.M. Dai, J.Y. Fu, C.C. Chen, Mol. Catal. 432 (2017) 196–209.
[48] Z. Ai, W. Ho, S. Lee, L. Zhang, Environ. Sci. Technol. 43 (2009) 4143–4150.
[49] Y.R. Jiang, S.Y. Chou, J.L. Chang, S.T. Huang, H.P. Lin, C.C. Chen, RSC Adv. 5 (2015) 30851–30860.
[50] L. Lin, S. Yuan, J. Chen, L. Wang, J. Wan, X. Lu, Chemosphere 78 (2010) 66–71.
[51] F. Dong, Y. Sun, M. Fu, Z. Wu, S.C. Lee, J. Hazard. Mater. 219–220 (2012) 26–34.
[52] A. Chatzitakis, C. Berberidou, I. Paspaltsis, G. Kyriakou, T. Sklaviadis, I. Poulios, Water Res. 42 (2008) 386–394.
[53] K. Ishibashi, A. Fujishima, T. Watanabe, K. Hashimoto, Electrochem. Commun. 2 (2000) 207–210.
[54] P. Pohla, Dissertation, Universität Regensburg, 2010.
[55] G. Giuseppetti, C. Tadini, Period. Miner. 42 (1973) 335–544.
[56] O.L. Stroyuk, O.Y. Rayevska, A.V. Kozytskiy, S.Y. Kuchmiy, J. Photochem. Photobiol. A 210 (2010) 209–214.
[57] C. Nasr, K. Vinodgopal, L. Fisher, S. Hotchandani, A.K. Chattopadhyay, P.V. Kamat, J. Phys. Chem. 100 (1996) 8436–8442.
[58] X. Xiao, R. Hao, M. Liang, X. Zuo, J. Nan, L. Li, W. Zhang, J. Hazard. Mater. 233–234 (2012) 122–130.
[59] N.M. Dimitrijevic, B.K. Vijayan, O.G. Poluektov, T. Rajh, K.A. Gray, H. He, P. Zapol, J. Am. Chem. Soc. 133 (2011) 3964–3971.
[60] J. Ma, C. Wang, H. He, Appl. Catal. B: Environ. 184 (2016) 28–34.
[61] W. Zou, L. Zhang, L. Liu, X. Wang, J. Sun, S. Wu, Y. Deng, C. Tang, F. Gao, L. Dong, App. Catal. B: Environ. 181 (2016) 495–503.
[62] D. Jiang, J. Li, C. Xing, Z. Zhang, S. Meng, M. Chen, ACS Appl. Mater. Interface 7 (2015) 19234–19242.
[63] Y. Tian, B. Chang, J. Lu, J. Fu, F. Xi, X. Dong, ACS Appl. Mater. Interfaces 5 (2013) 7079–7085.
[64] A.O. Kondrakov, A.N. Ignatev, V.V. Lunin, F.H. Frimmel, S. Bräse, H. Horn, Appl. Catal. B: Environ. 182 (2016) 424–430.
[65] W.W. Lee, C.S. Lu, C.W. Chuang, Y.J. Chen, J.Y. Fu, C.W. Siao, C.C. Chen, RSC Adv. 5 (2015) 23450–23463.
[66] X. Xiao, C. Xing, G. He, X. Zuo, J. Nan, L. Wang, Appl. Catal. B: Environ. 148–149 (2014) 154–163.
[67] H. Li, Y. Zhou, W. Tu, J. Ye, Z. Zou, Adv. Funct. Mater. 25 (2015) 998–1013.